Journal of Materials Chemistry A

PAPER

View Article Online
View Journal | View Issue

Cite this: J. Mater. Chem. A, 2014, 2, 5212

Synthesis of carbon nanomembranes through cross-linking of phenyl self-assembled monolayers for electrode materials in supercapacitors†

Youfu Wang, Rulin Xiong, Luhua Dong and Aiguo Hu*

Received 20th December 2013
Accepted 20th January 2014

DOI: 10.1039/c3ta15311h

www.rsc.org/MaterialsA

A bottom-up synthesis of three-dimensional (3D) carbon nanomembranes (CNMs) was developed through Friedel–Crafts cross-linking of phenyl self-assembled monolayers (SAMs) on silica nanospheres (SNSs) followed by high temperature treatment and template removal. The CNMs show a hierarchically 3D connected porous structure and the pore sizes are facilely tuned by varying the sizes of SNS templates. CNMs with high surface area (>1500 m^2 g^{-1}), large pore volume (~3 cm^3 g^{-1}) and partially graphitized frameworks exhibited good performances as supercapacitor electrode materials. The specific capacitance of the porous 3D CNMs reached 202 F g^{-1} at a current density of 0.5 A g^{-1} in an aqueous electrolyte.

1. Introduction

Challenges of environmental deterioration and the limited availability of fossil fuels have greatly affected the world economy and ecology. With a fast-growing market for portable electronic devices and the development of hybrid electric vehicles, there has been an ever increasing and urgent demand for environmentally friendly high-power energy resources. Electrochemical capacitors (EC), based on the electrochemical charge accommodation at the electric double layer (EDL) (in the case of EDL capacitors, EDLCs) and/or the occurrence of Faradaic reactions (in the case of pseudocapacitors), have attracted much attention because of their pulse power supply, long cycle life, simple principle, and high dynamic of charge propagation.[1–5] The development of electrode materials for high performance EDLCs has attracted much research interest in recent years, and porous carbon materials are regarded as first-candidate electrode materials for EDLCs owing to their high surface areas, tunable structures, and good conductivities.[6–12]

It is well acknowledged that the performance of an EDLC is related to the accessible specific surface area (SSA) of the porous electrode material.[1] Only the mass exposed to the electrolyte is able to contribute to storing electricity according to the Helmholtz equation. Following this line, ultrathin porous carbons including 3D graphene[13,14] have got more and more attention because of their more accessible and available mass than traditional carbon materials within which the carbon embedded inside cannot be fully used. 3D graphene can be formed either through chemical vapour deposition (CVD) on 3D skeletons[15] or by reduction of graphene oxide in the presence of pore-generating templates.[16,17] The success of 3D graphene in energy storage and electrical applications has encouraged the development of another kind of carbon material, carbon nanomembranes (CNMs).

CNMs are conductive membranes with a thickness of roughly one nanometre. They are generally formed by crosslinking of surface-bound monolayers of carbon-rich molecules. Gölzhäuser *et al.*[18–20] developed an approach to fabricate free-standing CNMs by stripping off hydrogen atoms of biphenyl self-assembled monolayers (SAMs) with electron irradiation. After annealing at high temperature, ultrathin, strong, conductive CNMs were obtained with nanocrystalline graphitic structures. Nishihara *et al.* introduced 2,3-dihydroxynaphthalene (DN) on the pore surface of SBA-15 (ref. 21) and mesoporous silica films (MSFs)[22] through the condensation of the hydroxyl groups of DN with the silanol groups of the silica at 573 K. The obtained carbon coated porous silica showed good electrical conductivity, but poor electric storage performance because the carbon coating could not self-support after the silica was removed.[23] Recently, we reported the fabrication of porous 3D CNMs through Bergman cyclization of enediyne SAMs on silica nanoparticles[24] and SBA-15.[25] The pore structure and pore size were varied by adjusting the texture parameters of the silica templates. The 3D CNMs exhibited large surface areas and good electrical conductivities, they were further used as catalyst supports in heterogeneous catalysis[26] and conductive supports for electrode materials in pseudocapacitors.[27] In this work, we developed a facile approach to bottom-up synthesize 3D CNMs through the Friedel–Crafts cross-linking reaction of phenyl SAMs

Shanghai Key Laboratory of Advanced Polymeric Materials, School of Materials Science and Engineering, East China University of Science and Technology, Shanghai, 200237, China. E-mail: hagmhsn@ecust.edu.cn; Fax: +86-21-64253037; Tel: +86-21-64253037

† Electronic supplementary information (ESI) available: Detailed experimental procedures and characterization by TEM, Raman, and BET. See DOI: 10.1039/c3ta15311h

on silica nanospheres (SNSs) followed by pyrolysis. The pore sizes of the CNMs were easily tuned by varying the sizes of the SNS templates. CNMs with high surface area (>1500 $m^2 g^{-1}$) and good conductivity showed good performances as supercapacitor electrode materials. The specific capacitance of the 3D CNMs reached 202 F g^{-1} at a current density of 0.5 A g^{-1} in an aqueous electrolyte.

2. Experimental section

Materials

Tetraethylorthosilicate (TEOS), $FeCl_3$ (anhydrous) and 1,2-dichloroethane (DCE) were obtained from National Medicines Corporation Ltd. of China. L-Lysine, phenyltriethoxysilane (PTES), and polytetrafluoroethylene (PTFE) were obtained from Aladdin Reagent Inc. Formaldehyde dimethyl acetal (FDA) was obtained from Alfa Aesar Co. All of these chemicals were of analytical grade and were used as received. Deionized water was used in all the experiments.

Synthesis of phenyl SAMs on SNSs (Ph-SNSs)

Ph-SNSs with different diameters and phenyl functional degrees were prepared in a one-pot reaction according to literature procedures[28,29] with minor modifications. In a typical synthesis of SNS-20-18, TEOS (50 mmol) was added to an L-lysine (1 mmol) solution in water (146 mL) at 90 °C with a stirring rate of 600 rpm. After 48 h, PTES (9 mmol) was added to the mixture in one portion and further stirred for 24 h. The suspension was hydrothermally aged at 100 °C for another 24 h without stirring and then filtered and dried under vacuum at 80 °C. The obtained white powder is denoted as SNS-*X*-*Y*, where *X* is the size of the SNSs and *Y* is the percentage phenyl functional degree (the molar ratio of PTES to TEOS). The SNS-10-*Y*s were synthesized by simply changing the reaction temperature to 60 °C and the reaction time to 24 h in the step of condensation of TEOS.

Cross-linking the phenyl groups on the surface of Ph-SNSs

Cross-linking of the phenyl groups was performed according to literature procedures through the Friedel–Crafts reaction.[30,31] In a typical cross-linking of SNS-20-18, FDA (45 mmol) was added to a mixture of SNS-20-18 (4 g) and $FeCl_3$ (45 mmol) in 200 mL DCE. After degassing by nitrogen bubbling, the mixture was stirred at 45 °C for 5 h to build up the preliminary polymeric network, and then heated at 80 °C for 19 h to complete the cross-linking. The resulting precipitate was washed three times with methanol and HCl (v/v = 15 : 1), then Soxhlet extracted with methanol for 24 h, and finally dried under reduced pressure at 60 °C for 24 h. The product is denoted as CL-SNSs.

Carbonization of CL-SNSs

Carbonization of CL-SNSs was performed in a tube furnace with a continuous mixed gas flow (H_2/Ar 10%). CL-SNSs were heated in the furnace from room temperature to 500 °C at a heating rate of 2 °C min^{-1} and kept for 2 hours and then to 900 °C and maintained for 1 h. After naturally cooling down to room temperature, a black powder was obtained, which is denoted as C-SNSs.

Removal of the SNS template

The removal process of the silica nanosphere template was performed in a polytetrafluoroethylene (PTFE) beaker with good ventilation. The obtained C-SNSs were treated with HF solution (40 wt%) to remove silica at ambient temperature. After washing with deionized water and drying under vacuum, CNMs were obtained as black powders, which are denoted as CNM-*X*-*Y*, where *X* and *Y* have the same meaning as stated above.

Characterization

Transmission electron microscopy (TEM) and high-resolution TEM images were taken using a JEOL TEM-1400 and JEOL TEM-2100 microscope operating at 100 kV and 200 kV, respectively. For the TEM measurements, samples were dispersed in absolute ethanol and then dried on a holey carbon film Cu grid. Raman measurements were performed on an inVia-reflex Raman spectrometer (Renishaw, 514 nm). Nitrogen sorption isotherms were obtained at 77 K using a Micromeritics Tristar 3000 analyser. Before measurements, the samples were degassed under vacuum at 200 °C for at least 6 h. The surface area of the samples was determined from the Brunauer–Emmett–Teller (BET) equation and analysed with the Barrett–Joyner–Halanda (BJH) method; the pore volumes and pore size distributions were derived from the desorption branches of isotherms.

Electrochemical tests

All the electrochemical measurements were done using a two-electrode setup with a titanium mesh coated with the CNMs as the working electrodes. For the preparation of working electrodes, 80 wt% of the CNM powder, 15 wt% of carbon black and 5 wt% of PTFE were mixed with a few drops of ethanol. After grinding for 2 hours, a homogeneous black slurry was obtained. Then, the mixture was tailored to a little circle slice (2–3 mg) and pressed onto a titanium mesh current collector (1 cm × 1 cm) and dried at 100 °C for 12 h to fabricate the electrode. Electrochemical performance was tested by cyclic voltammetry (CV), galvanostatic charge–discharge (CD) and electrochemical impedance spectroscopy (EIS) on a CHI 660D electrochemical workstation using two-electrode sandwich-type cell supercapacitors at room temperature. The cell supercapacitors were composed of two symmetrical working electrodes sandwiched by a separator and the aqueous electrolyte solution of 6 M KOH. The potential range for CV and CD experiments was 0–1 V. The EIS test was carried out in the frequency range of 10^5 to 10^{-2} Hz with 5 mV amplitude corresponding to open circuit potential. The cycling stability was tested using two-electrode cell supercapacitors on a LAND CT2001A program testing system.

The specific capacitances (C_s, F g^{-1}) of the electrode materials were obtained from the CD curves. The specific capacitance of the electrode can be calculated according to the following equation:

$$C_s = \frac{2I \times \Delta t}{m \times \Delta V}$$

where I (A) is the loaded current, Δt (s) is the discharge time, ΔV (v) is the potential drop during discharge, and m (g) is the mass of active material in a single electrode.

3. Results and discussion

Fig. 1a illustrates the preparation of the porous 3D CNMs from Ph-SNSs. The procedure consists of four steps: (i) formation of phenyl SAMs on silica nanospheres (Ph-SNSs) in a one-pot reaction, (ii) cross-linking the phenyl SAMs on Ph-SNSs through the Friedel–Crafts reaction, (iii) carbonization and (iv) removal of the silica template. The optical pictures of the material at each stage are shown in Fig. 1. The ultra-small spherical SNSs were synthesized with L-lysine as the catalyst and the structure-directing agent[28,32] in a weak basic solution (pH ≈ 9.2). Direct addition of PTES to the solution of the as-prepared SNSs allows the slow condensation of PTES to form phenyl SAMs on SNSs. The lysine molecules may serve as structure-directing agents in this step as well. With more PTES added at this stage, the SAMs are more compact and the final CNMs are stronger, until they are strong enough to self-support after the template removal. However, when a large amount of PTES is added, the excess PTES may self-condense to form gels. A considerable amount of precipitates appeared when the phenyl functional degree is over 20%. TEM images (Fig. 2a and b and S1†) of all these Ph-SNSs clearly illustrate this structural evolution. When the phenyl functional degree is below 20%, the Ph-SNSs are well separated by a clear interface between each other. When this ratio reaches 20%, TEM shows abundant agglomerates with a fuzzy interface. The cross-linking of phenyl SAMs on silica nanospheres was performed with a low-cost versatile Friedel–Crafts type "knitting" strategy recently developed by Tan *et al.*[30] Using $FeCl_3$ as a catalyst and FDA as a cross-linking agent, this reaction generates a rigid aromatic network in a facile manner, with the only by-product methanol. After the reaction, the nanospheres turned from white to brown (Fig. 1b and c), the same as many other microporous polymers, showing the complete cross-linking of the phenyl SAMs. After carbonization at 900 °C and silica removal, the final CNMs were obtained as black powders (Fig. 1e). Fig. 2c–d and S2† show TEM images of the 3D CNMs,

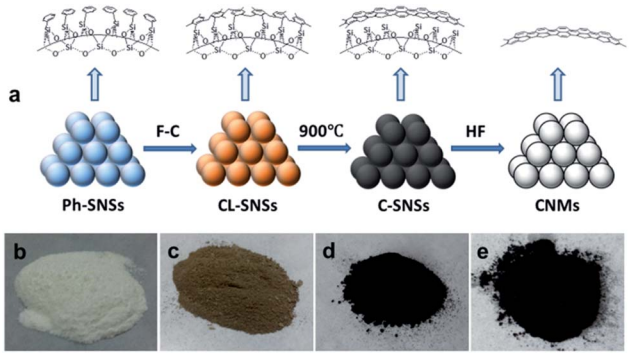

Fig. 1 Schematic illustration of the preparation of CNMs through cross-linking and carbonization of phenyl SAMs on SNSs (a) and optical pictures of the materials at each stage (b–e).

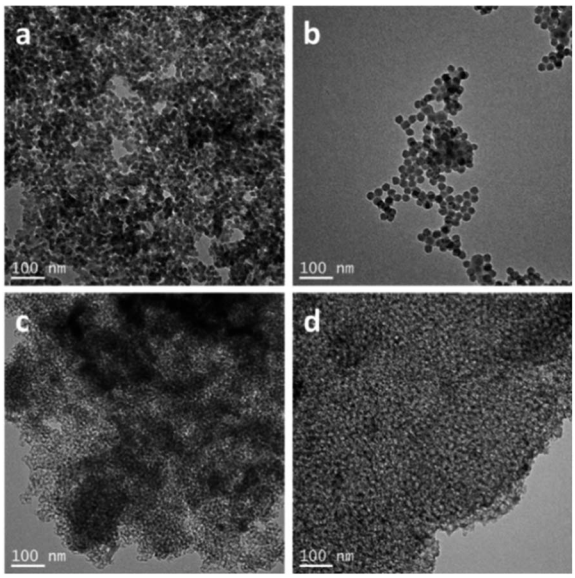

Fig. 2 TEM images of (a) SNS-10-18, (b) SNS-20-18, (c) CNM-10-18 and (d) CNM-20-18.

foam-like structures are present in all the samples with phenyl functional degrees between 10% and 20%. When this number is below 10%, no CNM was formed probably due to the incomplete formation of phenyl SAMs at the first stage. When this number reaches 20%, a structurally ill-defined matter appeared, which may have originated from the agglomerate of PTES self-condensate (*vida supra*). The high resolution TEM image (Fig. S3†) of CNM-10-18 clearly shows the foam structure and the partial graphitization of the pore wall.

Nitrogen sorption isotherms (Fig. 3a and S4†) of the porous CNMs show a representative type-IV curve with a hysteresis loop at high relative pressure. The amount of adsorbed N_2 gradually increased in the region of middle P/P_0 and increased in the region of high P/P_0 (>0.8 P/P_0) rapidly. This adsorption behaviour is attributed to the capillary condensation of N_2 in the mesopores of the porous CNMs between the adjacent hollow carbon cavities. With the increase of the phenyl functional degree during the formation of Ph-SNSs, the total pore volume of the CNMs first increases and then decreases, which illustrates the evolution of the porous structure of CNMs. The porous structure of the CNMs is gradually built-up with the improvement and perfection of the phenyl SAMs at the first stage, however, when an excess of PTES was added, the less porous carbon that originates from the self-condensate of PTES

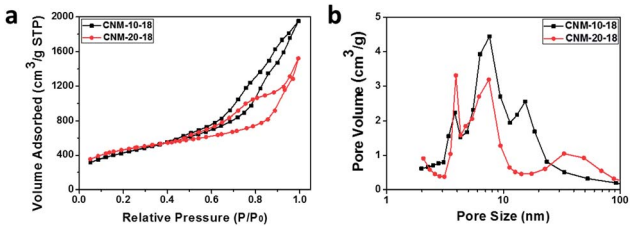

Fig. 3 (a) Nitrogen adsorption and desorption isotherms and (b) pore size distributions of CNM-10-18 (black line) and CNM-20-18 (red line).

(*vida supra*) appears, resulting in the decrease of the specific pore volume. The pore size distributions of the mesopores of the CNMs were calculated by the BJH method from the desorption branches. The hierarchical distribution of mesopores in a wide range is due to the intrinsic micropores of the CL-SNSs that expand to mesopores during carbonization, the adjacent hollow carbon cavities[33] and the expanding replica of the SNSs. Table 1 shows the texture parameters of these CNMs. The BET surface areas of the CNM-10-18 and CNM-20-18 are 1305 and 1521 $m^2\ g^{-1}$, respectively, and the total pore volume are 2.55 and 1.96 $cm^3\ g^{-1}$, respectively.

Raman spectroscopy was employed to examine the graphitization degrees of the CNMs. As shown in Fig. 4 and S5,† all of these CNMs exhibit similar curves, with two characteristic peaks at ~1339 and 1593 cm^{-1}, which correspond to the D and G bands of carbonous materials, respectively. It is well acknowledged that the D band is attributed to the defects, curved graphite sheets, and lattice distortions in carbon structures, whereas the G band is characteristic of the graphitic structure.[34] The fact that these samples with different sizes and different phenyl functionalization degrees show similar Raman spectra indicates that the graphitization degree of CNMs is independent of their morphology as they underwent a similar carbonization process. The intensity ratios I_D/I_G of these CNMs are around 0.95, suggesting a moderate degree of graphitization obtained during the carbonization process. Because of the low thickness of the carbon walls, the three-dimensional connected porous structure and moderate graphitization degree, all of these CNMs show high specific surface areas, large pore volumes and good conductivities, which are essential for the accommodation of the electrochemical charge for supercapacitor electrode materials.

The electrochemical performances of the porous CNMs were evaluated with cyclic voltammetry (CV) and galvanostatic charge–discharge (CD) tests. As shown in Fig. 5a, the CV curves of CNM-10-18 and CNM-20-18 at a high scan rate of 50 mV s^{-1} are characteristic of a relatively regular rectangle and a rapid current response to voltage reversal at each potential end. The obvious increase of current with the scan rate (Fig. S6a and S7a†) suggests good rate capabilities for these porous electrode materials. The CD curves of these CNMs (Fig. 5b, S6b and S7b†) at a current density of 1 A g^{-1} exhibit nearly mirror-like triangular-shaped charge–discharge curves with no perceptible voltage drop, both indicating typical electrical double-layer capacitance. Fig. 5c presents the specific capacitance as a function of the current density of CNM-10-18 and CNM-20-18. With the increase of current density from 0.5 to 20 A g^{-1}, CNM-10-18 exhibits specific capacitance from 143 to 104 F g^{-1}, with a capacitance retention of 72.7%, and CNM-20-18 shows specific capacitance from 202 to 132 F g^{-1}, with a capacitance retention of 65.3%. These high rate capabilities are essential for supercapacitors. Both of CNM-10-*Y* and CNM-20-*Y* series (Fig. S6c and S7c†) show an increase in the specific capacitance with the increase of the phenyl functional degree from 10% to 18% and then a decrease when excess of PTES (20%) was added at the first stage. This trend is consistent with the structural evolution observed in TEM and pore structure analysis, implying that the structural perfectness of the CNMs is important to their ability of accommodating the electrolyte ions. The larger the accessible surface area of the CNMs, the higher the capacitance, arguably agreed with the Helmholtz equation.

Electrochemical impedance spectroscopy (EIS) is a powerful tool to understand the fundamental behaviours of electrode

Table 1 Texture parameters of CNMs

Samples	Surface area ($m^2\ g^{-1}$)	Pore volume ($cm^3\ g^{-1}$)
CNM-10-10	1138.95	0.96
CNM-10-15	1095.24	1.17
CNM-10-18	1305.17	2.55
CNM-10-20	1238.36	2.07
CNM-20-10	1170.68	1.21
CNM-20-15	1331.71	2.86
CNM-20-18	1521.59	1.96
CNM-20-20	1315.69	1.96

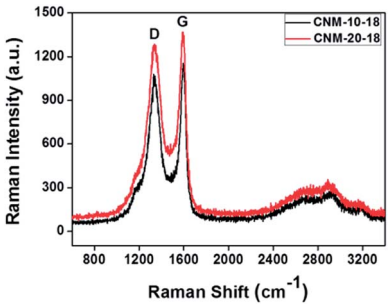

Fig. 4 (a) Raman spectra of CNM-10-18 (black line) and CNM-20-18 (red line).

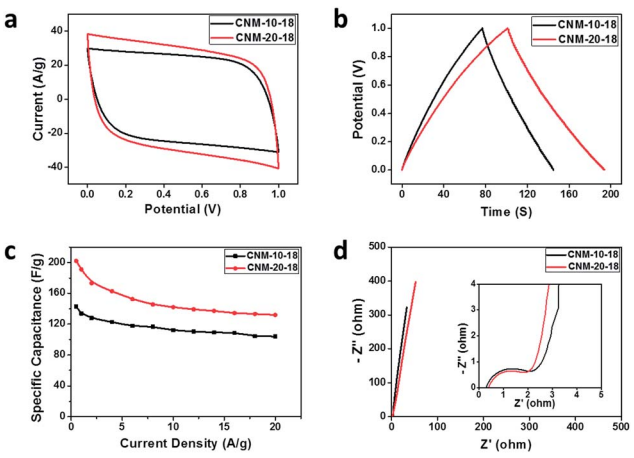

Fig. 5 Electrochemical capacitive behaviour of CNM-10-18 and CNM-20-18 measured in a two-electrode system by using a 6 M KOH aqueous solution as an electrolyte within the potential range: 0 to 1.0 V: (a) cyclic voltammetry curves at a scan rate of 50 mV s^{-1}, (b) galvanostatic charge–discharge curves at a current density of 1 A g^{-1}, (c) specific capacitance as a function of current density ranging from 0.5 to 20 A g^{-1}, (d) impedance Nyquist plots, the inset is a magnification of the high frequency region. All the calculations are based on the mass of the active material on a single electrode.

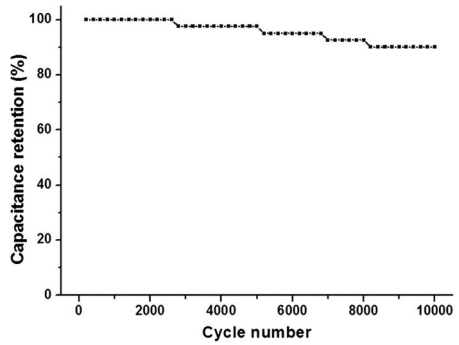

Fig. 6 Capacitance retention of CNM-20-18 measured at a current density of 4 A g^{-1} in a two-electrode system by using a 6 M KOH aqueous solution as the electrolyte.

materials. The EIS spectra of these porous CNMs are obtained in a frequency range of 100 kHz–0.01 Hz at open circuit potential with an alternating current perturbation of 5 mV. In the low frequency range, the straight line is attributed to the ion diffusion in the electrolyte, called the Warburg impedance. The linear parts (Fig. 5d) of CNM-10-18 and CNM-20-18 tend to be vertical lines while CNM-10-18 shows a larger Warburg slope, indicating the faster ion diffusion and higher capacitive retention in the CNM-10-18. At the high frequency end, the intercept at the real axis represents the ohmic resistance (R_S), including the ionic resistance of electrolyte, the intrinsic resistance of substrate and contact resistance. The semicircle corresponds to the charge transfer resistance (R_{CT}) at the electrode/electrolyte interface. The R_S of CNM-20-18 (0.39 Ω) is greater than that of CNM-10-18 (0.29 Ω), however, the R_{CT} of CNM-20-18 (1.58 Ω) is smaller than that of CNM-10-18 (1.81 Ω). The CNM-20-18 shows higher capacitance at low current density due to the faster charge transfer at the interface. When the current density increases, the higher ohmic resistance of CNM-20-18 hinders the dynamic accommodation of the hydrated ions at the surface of the electrode, resulting in lower capacitance retention at high current density.[33] The EIS of CNM-10-*Y*s and CNM-20-*Y*s series (Fig. S6d and S7d†) show similar ohmic resistance for these electrode materials probably due to the similar graphitization degrees. The charge transfer resistance decreases first and then increases with the increase of the phenyl functional degree in the first stage, consistent with the structural evolution (*vida supra*).

Fig. 6 shows the long-term cycling stability result of CNM-20-18 at a current density of 4 A g^{-1} in 6 M KOH solution. After 10 000 cycles, the capacitance retentions of CNM-20-18 are up to 90%. The high capacitance retention at high current density suggests that supercapacitors based on these 3D porous CNMs are able to function as long-term energy storage devices.

4. Conclusions

A series of 3D porous CNMs were synthesized through Friedel–Crafts cross-linking of phenyl SAMs on ultra-small SNSs followed by pyrolysis. TEM and pore structure analysis showed the structural evolution of CNMs with the phenyl functional degree at the first stage. When these numbers are between 10 and 18%, foam-like 3D porous CNMs were formed with high specific areas and large pore volumes. Raman spectroscopy showed that all these CNMs were carbonaceous materials with similar graphitization degrees. A supercapacitor material based on these CNMs exhibited a maximum specific capacitance of 202 F g^{-1} in aqueous electrolytes. After 10 000 consistent cycles, 90% retention of the initial capacitance was observed, suggesting the excellent electrochemical stability of these electrode materials, which are essential for supercapacitor applications.

Acknowledgements

The support of the National Natural Science Foundation of China (91023008), Ph.D. Programs Foundation of the Ministry of Education of China (20100074110002), the Fundamental Research Funds for the Central Universities, and the Shanghai Leading Academic Discipline Project (B502) is gratefully acknowledged. A.H. thanks Prof. Gengchao Wang for his help in electrochemical tests in this work.

Notes and references

1 P. Simon and Y. Gogotsi, *Nat. Mater.*, 2008, **7**, 845–854.
2 H. Zhang, G. Cao and Y. Yang, *Energy Environ. Sci.*, 2009, **2**, 932–943.
3 A. Izadi-Najafabadi, D. N. Futaba, S. Iijima and K. Hata, *J. Am. Chem. Soc.*, 2010, **132**, 18017–18019.
4 G. Wang, L. Zhang and J. Zhang, *Chem. Soc. Rev.*, 2012, **41**, 797–828.
5 J. Ren, L. Li, C. Chen, X. Chen, Z. Cai, L. Qiu, Y. Wang, X. Zhu and H. Peng, *Adv. Mater.*, 2013, **25**, 1155–1159.
6 F. Stoeckli and T. A. Centeno, *J. Mater. Chem. A*, 2013, **1**, 6865–6873.
7 L. Hao, X. Li and L. Zhi, *Adv. Mater.*, 2013, **25**, 3899–3904.
8 C. R. Pérez, S.-H. Yeon, J. Ségalini, V. Presser, P.-L. Taberna, P. Simon and Y. Gogotsi, *Adv. Funct. Mater.*, 2013, **23**, 1081–1089.
9 H. Nishihara and T. Kyotani, *Adv. Mater.*, 2012, **24**, 4473–4498.
10 Y. Liang, F. Liang, H. Zhong, Z. Li, R. Fu and D. Wu, *J. Mater. Chem. A*, 2013, **1**, 7000–7005.
11 Z. Li, L. Zhang, B. S. Amirkhiz, X. Tan, Z. Xu, H. Wang, B. C. Olsen, C. M. B. Holt and D. Mitlin, *Adv. Energy Mater.*, 2012, **2**, 431–437.
12 M. G. Hahm, A. Leela Mohana Reddy, D. P. Cole, M. Rivera, J. A. Vento, J. Nam, H. Y. Jung, Y. L. Kim, N. T. Narayanan, D. P. Hashim, C. Galande, Y. J. Jung, M. Bundy, S. Karna, P. M. Ajayan and R. Vajtai, *Nano Lett.*, 2012, **12**, 5616–5621.
13 B. G. Choi, M. Yang, W. H. Hong, J. W. Choi and Y. S. Huh, *ACS Nano*, 2012, **6**, 4020–4028.
14 Z.-S. Wu, Y. Sun, Y.-Z. Tan, S. Yang, X. Feng and K. Müllen, *J. Am. Chem. Soc.*, 2012, **134**, 19532–19535.
15 H. M. Cheng, Z. P. Chen, W. C. Ren, L. B. Gao, B. L. Liu and S. F. Pei, *Nat. Mater.*, 2011, **10**, 424–428.
16 X. D. Huang, K. Qian, J. Yang, J. Zhang, L. Li, C. Z. Yu and D. Y. Zhao, *Adv. Mater.*, 2012, **24**, 4419–4423.

17 L. Zhang, F. Zhang, X. Yang, G. K. Long, Y. P. Wu, T. F. Zhang, K. Leng, Y. Huang, Y. F. Ma, A. Yu and Y. S. Chen, *Sci. Rep.*, 2013, **3**, 1408.
18 W. Eck, A. Küller, M. Grunze, B. Völkel and A. Gölzhäuser, *Adv. Mater.*, 2005, **17**, 2583–2587.
19 A. Turchanin, A. Beyer, C. T. Nottbohm, X. H. Zhang, R. Stosch, A. Sologubenko, J. Mayer, P. Hinze, T. Weimann and A. Golzhauser, *Adv. Mater.*, 2009, **21**, 1233–1237.
20 A. Golzhauser, *Angew. Chem., Int. Ed.*, 2012, **51**, 10936–10937.
21 H. Nishihara, Y. Fukura, K. Inde, K. Tsuji, M. Takeuchi and T. Kyotani, *Carbon*, 2008, **46**, 48–53.
22 H. Nishihara, T. Kwon, Y. Fukura, W. Nakayama, Y. Hoshikawa, S. Iwamura, N. Nishiyama, T. Itoh and T. Kyotani, *Chem. Mater.*, 2011, **23**, 3144–3151.
23 T. Kwon, H. Nishihara, Y. Fukura, K. Inde, N. Setoyama, Y. Fukushima and T. Kyotani, *Microporous Mesoporous Mater.*, 2010, **132**, 421–427.
24 Z. Li, D. Song, J. Zhi and A. Hu, *J. Phys. Chem. C*, 2011, **115**, 15829–15833.
25 X. Yang, Z. Li, J. Zhi, J. Ma and A. Hu, *Langmuir*, 2010, **26**, 11244–11248.
26 J. Zhi, D. Song, Z. Li, X. Lei and A. Hu, *Chem. Commun.*, 2011, **47**, 10707–10709.
27 J. Zhi, S. Deng, Y. Zhang, Y. Wang and A. Hu, *J. Mater. Chem. A*, 2013, **1**, 3171–3176.
28 T. Yokoi, Y. Sakamoto, O. Terasaki, Y. Kubota, T. Okubo and T. Tatsumi, *J. Am. Chem. Soc.*, 2006, **128**, 13664–13665.
29 T. Yokoi, J. Wakabayashi, Y. Otsuka, W. Fan, M. Iwama, R. Watanabe, K. Aramaki, A. Shimojima, T. Tatsumi and T. Okubo, *Chem. Mater.*, 2009, **21**, 3719–3729.
30 B. Li, R. Gong, W. Wang, X. Huang, W. Zhang, H. Li, C. Hu and B. Tan, *Macromolecules*, 2011, **44**, 2410–2414.
31 R. Dawson, L. A. Stevens, T. C. Drage, C. E. Snape, M. W. Smith, D. J. Adams and A. I. Cooper, *J. Am. Chem. Soc.*, 2012, **134**, 10741–10744.
32 W. Fan, M. A. Snyder, S. Kumar, P.-S. Lee, W. C. Yoo, A. V. McCormick, R. Lee Penn, A. Stein and M. Tsapatsis, *Nat. Mater.*, 2008, **7**, 984–991.
33 A. Vu, X. Li, J. Phillips, A. Han, W. H. Smyrl, P. Bühlmann and A. Stein, *Chem. Mater.*, 2013, **25**, 4137–4148.
34 T. Hiraoka, S. Bandow, H. Shinohara and S. Iijima, *Carbon*, 2006, **44**, 1853–1859.